Full length article

Development of more efficient cold-formed steel channel sections in bending

CrossMark

Jun Ye *, Iman Hajirasouliha, Jurgen Becque, Kypros Pilakoutas

Department of Civil and Structural Engineering, The University of Sheffield, Sheffield, UK

ABSTRACT

Cold-formed steel (CFS) cross-sections can be optimised to increase their load carrying capacity, leading to more efficient and economical structural systems. This paper aims to provide a methodology that would enable the development of optimised CFS beam sections with maximum flexural strength for practical applications. The optimised sections are designed to comply with the Eurocode 3 (EC3) geometrical requirements as well as with a number of manufacturing and practical constraints. The flexural strengths of the sections are determined based on the effective width method adopted in EC3, while the optimisation process is performed using the Particle Swarm Optimisation (PSO) method. To allow for the development of a new 'folded-flange' cross-section, the effective width method in EC3 is extended to deal with the possible occurrence of multiple distortional buckling modes. In total, ten different CFS channel cross-section prototypes are considered in the optimisation process. The flexural strengths of the optimised sections are verified using detailed nonlinear finite element (FE) analysis. The results indicate that the optimised folded-flange section provides a bending capacity which is up to 57% higher than standard optimised shapes with the same amount of material.

1. Introduction

Cold-formed steel (CFS) cross-sections are used extensively in the construction industry as secondary load-carrying members, such as roof purlins and wall girts. In recent years, however, CFS cross-sections are also increasingly being employed as primary structural elements. For example, CFS framing systems are used in low- to mid-rise multi-storey buildings [1] and CFS portal frames are gaining popularity in single-storey industrial buildings with short to intermediate spans [2,3]. In both cases, CFS members are employed as the primary load-bearing members and consequently have to meet increased demands in terms of span length and load-carrying capacity. Compared to hot-rolled members, CFS thin-walled members offer several advantages of economy and efficiency, including a high strength for a light weight, a relatively straightforward manufacturing process and an ease of transportation and erection. Above all, CFS sections offer flexibility and versatility in producing a variety of cross-sectional shapes, which are obtained by bending relatively thin metal sheets using either a cold-rolling or a press-braking process at room temperature. Fig.1 illustrates this by showing a series of relatively complex commercially available CFS sections and profiled sheets. The flexibility

of the manufacturing process in obtaining various shapes means that there is a great potential for CFS sections to be optimised to meet specific objectives, thereby bringing practical benefits to both manufacturers and structural designers.

Due to their typically large flat width-to-thickness ratios, CFS sections are inherently susceptible to local, distortional and global buckling modes, resulting in a complex optimisation process. Previous studies on the optimisation of CFS elements have mainly been limited to varying the dimensions of standard cross-sections such as lipped channel beams [4], channel columns with and without lips [5,6] and hat, I- and Z- cross section CFS beams [7]. Taking the elastic buckling strength as an optimisation criterion, Magnucki et al. [8,9] developed optimum CFS beams with a mono-symmetrical open cross-section and sinusoidally corrugated flanges, as well as optimum I-shaped sections with box-shaped flanges. A CFS channel beam with closed hollow flanges was proposed and optimised with respect to its member capacity by Magnucka-Blandzi [10]. Analytical formulas were thereby developed to calculate the local and global buckling strengths in a process to obtain feasible solutions in a design space constrained by geometric conditions. The results of their study indicated a better flexural performance compared to the traditional lipped or plain channel sections. More recently, CFS compression and bending members [11,12] were optimised with respect to their capacity according to EC3 [13] using Genetic Algorithms. The researchers investigated the influence of the column length and the shift of the effective
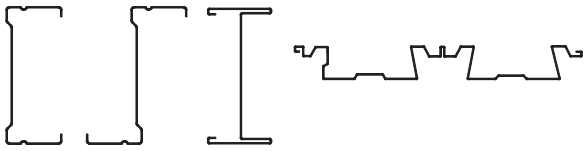
Fig. 1. Examples of commercially available CFS sections with complex shapes.
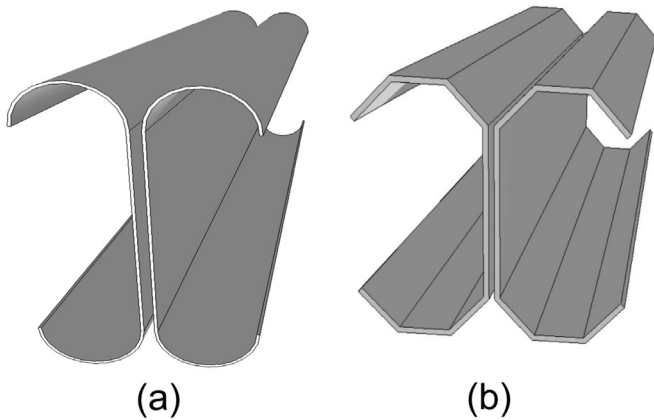

Fig. 2. CFS beams with (a) curved flanges and (b) folded flanges.

centroid, induced by local/distortional buckling, on the optimal design solutions. The shapes of the cross-section were thereby limited to the conventionally used lipped channels.

In order to obtain 'global optimum' solutions, research at Johns Hopkins University and Griffith University was conducted on the free form optimisation of CFS cross-sections without placing any prior constraints on the shape of the cross-section. The finite strip method (FSM) and the direct strength method (DSM [14]) were thereby combined with Genetic Algorithms (GA) to obtain optimum shapes for open CFS cross section columns [15–17]. While this led to some innovative new geometries, the resulting cross-sections were not 'pre-qualified' according to the DSM approach, thus casting some doubt on the optimisation procedure. Additionally, these studies did not consider any manufacturing or construction constraints and, therefore, highly complex shapes were obtained which cannot be deemed suitable for practical applications due to a complex (or unfeasible) manufacturing process and the obvious difficulty in connecting the cross-section to other elements. Leng et al. [18] later advanced this work by incorporating some end-user constraints and by limiting the numbers of rolling passes in the manufacturing process. CFS columns with different lengths were optimised and more practical shapes were obtained, which, however, still did not meet the DSM pre-qualification criteria.

Recent experimental and numerical research on CFS moment resisting connections [19] at the University of Sheffield has demonstrated that CFS channel sections with curved flanges (Fig. 2a) display a higher flange buckling load and also possess higher strength, stiffness and ductility compared to channels with flat flanges. However, this type of cross-section is difficult to connect to a typical floor system, allowing just a point contact. Practically, the curved flange can be substituted with a folded flange which approximates it, as shown in Fig. 2(b). However, the EC3 guidelines [13,20,21] do not provide a direct procedure for the design of such cross-sections. In particular, there is a need to develop a design procedure that can account for the multiple distortional buckling modes which may occur in the folded-flange section. This study aims to develop such a design methodology in order to subsequently use it to optimise the CFS folded-flange section. The efficiency of the folded-flange beam section is investigated alongside nine more conventional channel prototypes which are aimed at investigating the effects of intermediate web stiffeners, return lips and inclined lips. All sections are optimised by maximising the cross-sectional flexural capacity for a given thickness and coil width (equal to the total developed length of the cross-section). A brief overview of the effective width method adopted in EC3 [13] is first given in Section 2. This method is then extended to deal with the presence of multiple distortional buckling modes in the folded-flange cross-section. The particle swarm optimisation (PSO) method, used to solve the optimisation problem, is described in Section 3 and the optimum solutions are presented in Section 4. The accuracy of the proposed design model and the efficiency of the optimisation procedure are investigated through detailed nonlinear FE modelling in Section 5. A comprehensive comparison of the optimised results is provided in Section 6.

2. Design of CFS members based on EC3

The CFS sections to be optimised are evaluated according to the cross-sectional strength and stability provisions in EN1993-1-3 (EC3) [13] accounting for both local and distortional buckling modes. The "notional flat widths" [19] of the plate assemblies are used to determine the cross-sectional properties, which are then reduced by a factor (δ) to account for the influence of the rounded corners. A brief description of the EC3 provisions for the design of CFS members is provided in the following subsections.

2.1. Local buckling

In EC3, the effect of local buckling is considered through the effective width concept. It recognises the fact that local buckling of the plates constituting the cross-section has the effect of shifting the load-bearing stresses towards the corner zones, in the process
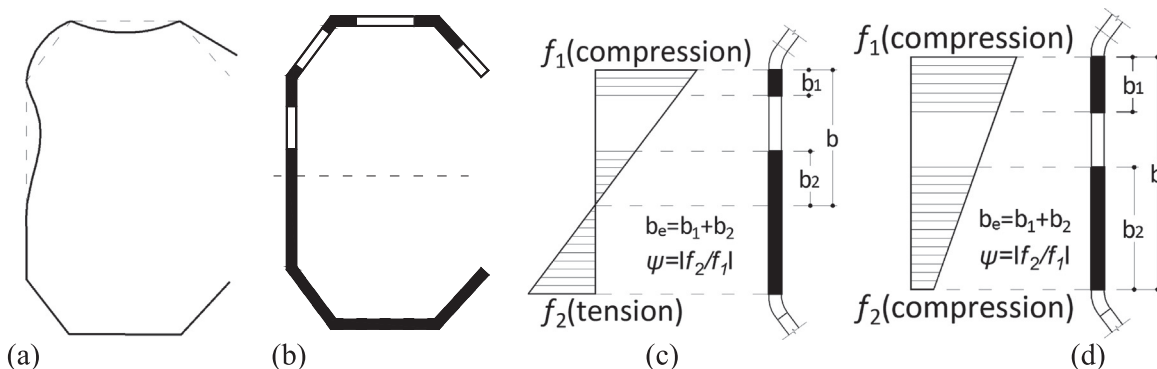

Fig. 3. Local buckling mode of a folded-flange cross-section: (a) buckled shape, (b) effective area of the cross-section for local buckling, (c, d) web under stress gradient.

reducing the effectiveness of the central parts in carrying compressive stresses. The cross-section is consequently idealised as an "effective cross-section", shown in solid black line in Fig. 3(b). This effective area is assumed to resist the full bending action applied to the section. According to Eurocode 3, Part 1–5 [21], the effective width of a (doubly supported) plate is given by:

$$\frac{b_e}{b} = \frac{1}{\lambda_l}\left(1 - \frac{0.055(3 + \psi)}{\lambda_l}\right) \tag{1}$$

with $\lambda_l = \sqrt{\dfrac{f_y}{\sigma_{cr}}}$ (2)

and $\sigma_{cr} = \dfrac{k\pi^2 E t^2}{12\left(1 - v^2\right)b^2}$ (3)

where b and b_e are the total and the effective width of the plate, respectively. $\psi = f_2/f_1$ is the stress ratio of the plate, as shown in Fig.3(c) and (d). An equation similar to Eq. (1) is also provided for outstand elements. The slenderness ratio for local buckling, λ_l, relates the material yield stress, f_y, to the elastic local buckling stress of the plate, σ_{cr}. In Eq. (3), v and E are the Poisson's ratio and the Young's modulus of the plate, respectively, and k is the buckling factor calculated using Eurocode 3, Part 1–5 [21] based on the boundary conditions and the stress ratio ψ. For a doubly supported plate subjected to uniform compression $k=4$, while for an outstand element under uniform compression $k=0.43$. The Eurocode thus assumes, for the purpose of calculating σ_{cr}, that every plate element is simply supported along its fold-lines, neglecting any interaction with adjacent plates. It is also worth noting that, in principle, the Eurocode always calculates the effective cross-section, W_{eff}, based on the yield stress, f_y, while some other design standards (e.g. the AISI [14] and AS/NZS [22] specifications) use the stress at global buckling.

2.2. Distortional buckling

Distortional buckling of CFS members is linked to any buckling mode causing a distortion of the shape of the cross-section, but excludes those deformations related to local buckling (Fig. 4(a)). As a result, distortional buckling is always associated with the displacement of one or more of the fold-lines of the section out of their original positions. Distortional buckling can also be interpreted as global (flexural or flexural-torsional) buckling of plate subassemblies within the cross-section. In line with this latter view, EC3 [13] bases the design for distortional buckling on the assumption that the plate subassembly at risk of buckling (which could be a stiffened web or a compressed flange-lip assembly)

behaves as a strut continuously supported by elastic springs of stiffness K along its centroid axis. These springs replace the restraint experienced by the plate assembly from the omitted parts of the cross-section and therefore depend on the flexural stiffness of the adjacent plates. The buckling behaviour can then be studied by considering an equivalent strut on an elastic foundation, as shown in Fig. 4(b). The elastic critical buckling stress of the strut $\sigma_{cr,s}$ is:

$$\sigma_{cr,s} = \frac{2\sqrt{KEI_s}}{A_s} \tag{4}$$

where E is the Young's modulus, I_s is the second moment of the area of the stiffener about the axis through its centroid parallel to the plate element being stiffened, K is the spring stiffness per unit length, and A_s is the effective cross-sectional area of the edge stiffener. The stiffness K is determined by applying a unit load $u=1$ (per unit length) at the centroid of the effective part of the edge stiffener assembly, as shown in Fig. 4(a) for the case of a double-fold stiffener. The stiffness of the equivalent springs thus depends on the flexural stiffness of the adjacent plane elements.

This procedure cannot directly be applied to the design of the folded-flange cross-section shown in Fig. 2(b), because of the possibility of not one, but two distinctively different distortional buckling modes occurring, depending on the relative lengths of the flange segments. As illustrated in Fig. 5, when the length of flange segment 2 is relatively large compared to segment 1, distortional buckling type 1 is dominant (i.e. buckling of the assembly consisting of flange segment 2 and the lip). However, for sections where flange segment 1 is much longer than segment 2, distortional buckling of type 2 (illustrated in Fig. 6) is critical (i.e. buckling of the assembly consisting of flange segments 1 and 2 and the lip). Considering the two structural systems shown in Figs. 5 and 6 (and ignoring any second order effects), the deflections δ_1 and δ_2 produced by concentrated forces u_1 and u_2, respectively, can be determined to be:

$$\delta_1 = \frac{u_1}{3D}\Big[e^3 + e^2 b + b(e - b\cos\theta_1)(2e - b\cos\theta_1) \\ + \frac{3}{2}h(e - b\cos\theta_1)^2\Big] \tag{5}$$

$$\delta_2 = \frac{u_2}{3D}\Big[e^3 + \frac{3}{2}he^2\Big] \tag{6}$$

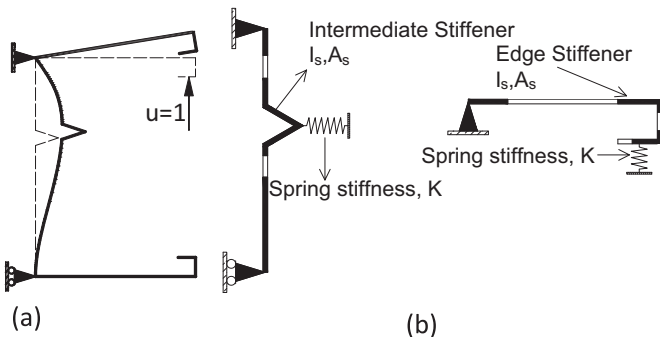where the bending rigidity of the plate, D, is determined by:

Fig. 4. Distortional buckling mode of a channel section with intermediate and edge stiffeners (a) distortionally buckled shape and (b) equivalent struts.
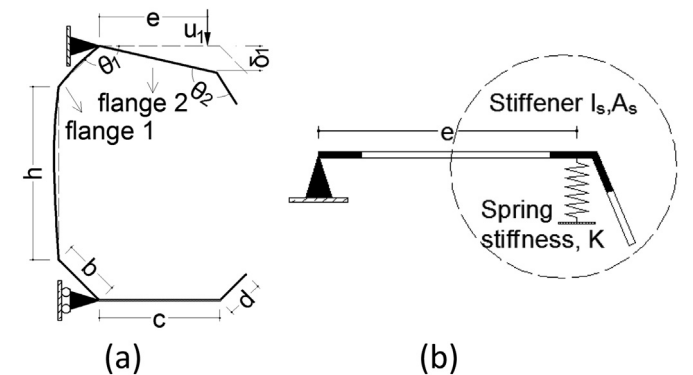

Fig. 5. (a) Actual system, and (b) simplified model to analyse distortional buckling of type 1.
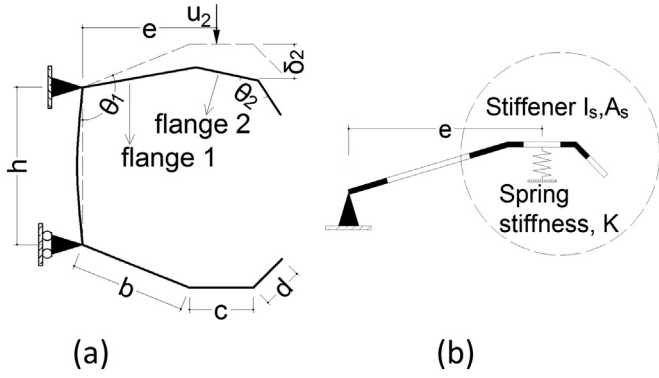
Fig. 6. (a) Actual system, and (b) simplified model to analyse distortional buckling of type 2.

$$D = Et^3/12\left(1 - v^2\right) \tag{7}$$

In the above equations, e is the distance between the centroid of the edge stiffener (shown in Figs. 5(b) and 6(b)) and the pivot point (which is the web-to-flange junction for type 2 buckling and the junction between flange segments 1 and 2 for type 1 buckling), h is the height of the web, b is the length of flange segment 1 and θ_1 is the angle between flange segment 1 and segment 2 (see Figs. 5(a) and 6(a)). Furthermore, t is the plate thickness and E and v are the modulus of elasticity and the Poisson's ratio, respectively.

Distortional buckling is taken into account in EC3 [13] using a reduction factor X_d on the thickness of the stiffeners. This method can be extended to deal with folded-flange cross-sections by determining the elastic distortional buckling stress $\sigma_{cr,s}$, with Eq. (4), using a stiffness K obtained from Eqs. (5 and 6) as $K=u/\delta$. The effective cross-section needs to be calculated separately for each of the two distortional modes, yielding two effective cross-section moduli. For a particular cross-section, the effective section modulus is then taken as the minimum value of the two.

The design model developed for the folded-flange section is further used during the optimisation process in Sections 3 and 4.

3. Description of the particle swarm optimisation process

Particle swarm optimisation (PSO) is a population-based method which is inspired by the swarming behaviour of biological populations such as the motion of bird flocks or schools of fish [23]. Its mechanism has some parallels with evolutionary computation techniques, such as Genetic Algorithms (GA). An initial population of solutions is randomly generated, but unlike GA, solutions are optimised by updating generations without any evolution operators such as crossover or mutation. The potential solutions in PSO, called particles, move in the problem space by following the current optimum particles. This usually leads to a better efficiency in terms of computational time and cost and, therefore, a faster convergence rate compared to GA [24,25].

A swarm comprises of N particles moving around a D-dimensional search space, in which each particle represents a potential solution to the optimisation problem. The position and velocity vectors of ith particle are $\rho_i = \{\rho_{i1}, \rho_{i2}, \dots, \rho_{ij}, \dots, \rho_{iD}\}$ and $V_i = \{v_{i1}, v_{i2}, \dots, v_{ij}, \dots, v_{iD}\}$, respectively, where $i = 1, 2, 3, \dots N$. The particles fly through the feasible region in search for the global optimal solution. In each iteration step, the ith particle updates its position and velocity based on a combination of: (a) its personal best position over its history, and (b) the position of the particle within the swarm with the best position in the previous iteration. This can mathematically be expressed as:

$$V_i^{k+1} = w \cdot V_i^k + c_1 \cdot r_1 \cdot \left(P_{\text{best},i}^k - \rho_i^{\ k}\right)/\Delta t + c_2 \cdot r_2 \cdot \left(G_{\text{best}}^k - \rho_i^{\ k}\right)/\Delta t \tag{8}$$

$$\rho_i^{k+1} = \rho_i^{\ k} + V_i^{k+1} \cdot \Delta t \tag{9}$$

where the subscripts i and k denote the particle and the iteration number, respectively, and Δt is the time increment. The vectors $P_{best,i} = \{p_{i1}, p_{i2}, \dots, p_{ij}, \dots, p_{iD}\}$ and $G_{best} = \{g_1, g_2, \dots, g_j, \dots, g_D\}$ denote the best position of the ith particle over its history up to iteration k, and the position of the best particle in the swarm in iteration k, respectively. Also, c_1 is a cognitive parameter indicating the degree of confidence in the solution $P_{\text{best},i}$ obtained from each individual particle, whereas c_2 is a social parameter to reflect the confidence level that the swarm as a whole has reached a favourable position. In addition, r_1 and r_2 are two independent random numbers uniformly distributed between 0 and 1, adding a random searching aspect within the feasible region, and w is the inertial weight factor used to preserve part of the previous velocity of the particles. According to Perez [26], the convergence conditions for PSO can be expressed as:

$$0 < c_1 + c_2 < 4 \tag{10}$$

$$\frac{c_1 + c_2}{2} - 1 < w < 1 \tag{11}$$

To improve the global versus local search behaviour, a dynamic variation of the inertial weight is used in this study by linearly decreasing w with successive iterations as follows [27]:

$$w_{k+1} = w_{\text{max}} - \frac{w_{\text{max}} - w_{\text{min}}}{k_{\text{max}}} k \tag{12}$$

where k_{max} is the total iteration number and w_{max} and w_{min} are the maximum and minimum values of the inertial weight factor, respectively.

4. Optimisation procedure

4.1. Problem definition

The optimisation procedure in this study aimed to maximise the bending capacity of CFS cross-sections. The optimisation problem can thus be formulated as:

$$\max\left(M_{c,Rd} = W_{eff}(x) \cdot f_y\right) \quad d_{\min} \le x_i \le d_{\max} \text{ for } i = 1, \dots, N \tag{13}$$

where $M_{c,Rd}$ is the moment resistance of a cross-section about its major axis and $W_{eff}(x)$ is the effective section modulus. The effective section modulus W_{eff} is calculated about the major principal axis through the centroid of the effective area. The effective width and the effective thickness of each plate element are first calculated according to the procedure outlined in Sections 2.1 and 2.2 to account for both local and distortional buckling. The effective second moment of area of the cross section I_{eff} is then computed from the contributions of all effective parts of the cross-section and divided by the maximum distance from the effective centroid to the edge of the cross-section to obtain W_{eff}. For each design variable, x_i, lower and upper bounds, $d_{\min}$ and $d_{\max}$, were determined based on a combination of the constraints imposed by EC3 [13] and certain manufacturing limitations and practical considerations, which will be explained further in this section. Throughout the optimisation process, the thickness of the cross-sections was kept constant at 1.5 mm and the total developed length of the cross-section (the coil width) was also maintained at 415 mm. These values were taken from a commercially available channel section, shown in Fig. 7, which was used as a benchmark
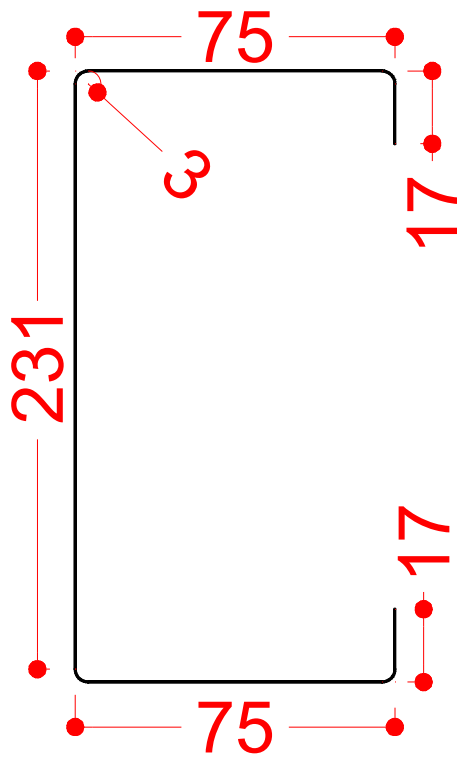
Fig. 7. Selected commercial CFS beam cross-section (dimensions in mm).

and to which the performance of the optimised sections will be compared in Section 4.2.

The values of the radius of the rounded corners (measured along the heart-line), the elastic modulus and the Poisson's ratio were taken as 3 mm, 210 GPa and 0.3, respectively. The yield stress of the CFS material was assumed to be $f_y = 450$ MPa. It is again noted that the optimisation was carried out with respect to the cross-sectional capacity, excluding lateral-torsional buckling. This situation is representative, for instance, of purlins connected to a steel deck with concrete topping, where the compression flange is continuously supported, or even of roof purlins where the lateral and rotational stiffness of the roof diaphragm and/or the presence of sufficient bridging prevent any out-of-plane effects.

To ensure the practicality of the optimised sections, the following additional constraints were imposed:

(1) The basic overall shape of all the cross-sections was restricted to a channel. Channel sections are currently the most widely used CFS beams in practical applications. The fact that they are composed of flat plate elements both allows for a straightforward manufacturing process and facilitates the connections to trapezoidal steel decking or roof/wall systems, as well as bridging, cleat plates, etc… Ten different prototypes were optimised, which are shown in Table 1. They include nine relatively conventional sections and the newly proposed folded-flange channel section. All prototypes are based on a channel shape, but they allow the addition of a single web stiffener, double web stiffeners, inclined lips and double-fold (return) lips. These features are commonly encountered within commercially available sections and do not impose any excessive demands on the fabrication process. Each prototype was individually optimised, after which the overall optimum among the ten optimised prototypes was identified.

(2) In practice, additional constraints of a very concrete nature typically come into play. These constraints may be quite case-

dependent and may, for instance, be related to the ability to connect the beam to other elements, or be imposed by the manufacturing process itself. In this particular case, the following constraints were imposed:

a) The width of the flanges was required to be at least 50 mm in order to connect trapezoidal decking or plywood boards to the beam by means of screws. This width was determined after consultation with the industrial partner on the project. In the case of the folded flange section, it was the flat width of the central horizontal segment which was restricted to a minimum of 50 mm.

b) The lip needs to be of a sufficient length. A lip of, for instance, 1 mm length cannot be rolled or brake-pressed. The industrial partner on the project suggested a minimum length of 5–15 mm. Therefore, as indicated in Table 1, $c \geq 15$ mm was imposed for a single lip and combined with $d \geq 5$ mm for a return lip.

c) The height of the web was specified to be at least 100 mm in order to allow a connection to be made (e.g. to a cleat plate) with at least two bolts and/or for bridging to be installed. An upper bound of 350 mm was also imposed limit the total floor depth.

d) The ratio R (see Table 1) was restricted so that the intermediate web stiffener would be physically positioned within the web.

One of the major advantages of the PSO algorithm is that these constraints can easily be accommodated and others added. The constraints merely result in a restriction of the search space of the particle swarm.

In addition to the practical constraints mentioned above, the EC3 design rules [13] also impose certain limits on the plate width-to-thickness ratios, the relative dimensions of the cross-section and the angle of the edge stiffeners. These constraints were also taken into account in the optimisation procedure and are listed in Table 1 under the heading 'Constraints based on EC3'.

Finally, the opening angle and the leg length of the intermediate stiffeners were limited to $\pi/6$ and 15 mm, respectively.
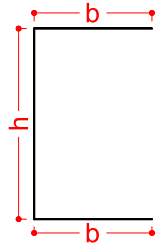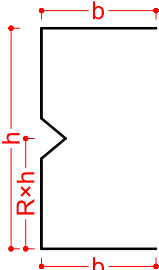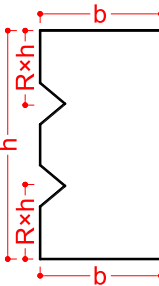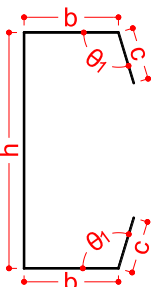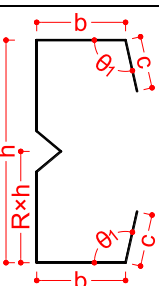
4.2. Optimisation solutions

To facilitate the optimisation process, both the design procedure and the optimisation algorithm were implemented in Matlab [28]. The population size of the particle swarm N was taken as 100, and 100 iterations k_{max} were used to obtain the optimum results. The maximum and minimum inertial weight factors w_{max} and w_{min} were taken as 0.95 and 0.4, respectively, as recommended in [27]. Each of the prototypes was optimised 3 times using a different set of random initial particles and the result with the maximum bending capacity was retained as the optimum section. As an example, Fig. 8 shows the iteration history of the bending capacity of prototype ⑩, where the convergence was practically achieved after about 50 steps.
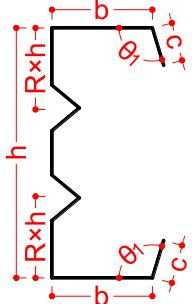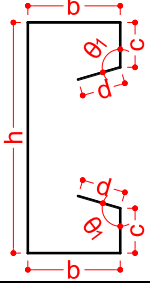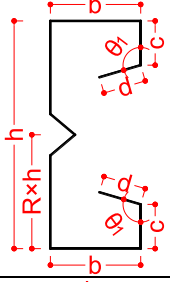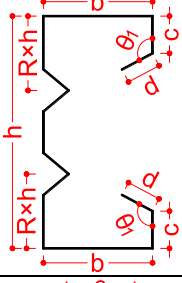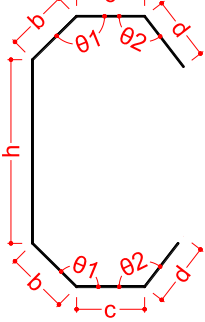
Table 2 summarises the dimensions and the bending capacity of the optimised cross-sections corresponding to each of the prototypes presented in Table 1. Table 3 illustrates the effective cross-section of the optimised prototypes, maintaining the same scale for all cross-sections. A thick black line represents a fully effective part of the cross-section, while a line with intermediate thickness indicates that the thickness has been reduced to account for distortional buckling.

It is clear from Table 3 that, in general, the optimised cross-sections tend to adopt the minimum specified flange width of 50 mm and, hence, have a large height-to-width ratio. However, prototypes ① to ③, which have the largest height, still show the

Table 1
Selected prototypes, design variables and constraints.

Prototype	Prototype section	Design variables	Constraints based on EC3	Manufacturing & practical limitations
①		$x=c/b$	$b/t\leq50$ $h/t\leq500$	$b\geq50$ $100\leq h\leq350$
②		$x_1=c/b$ $x_2=b/L$ $x_3=R$	$b/t\leq50$ $h/t\leq500$	$b\geq50$ $100\leq h\leq350$ $0.1\leq R\leq0.9$
③		$x_1=c/b$ $x_2=b/L$ $x_3=R$	$b/t\leq50$ $h/t\leq500$	$b\geq50$ $100\leq h\leq350$ $0.1\leq R\leq0.9$
④		$x_1=c/b$ $x_2=b/L$ $x_3=\vartheta_1$	$0.2\leq c/b\leq0.6$ $b/t\leq60$ $c/t\leq50$ $h/t\leq500$ $\pi/4\leq\vartheta_1\leq3/4\pi$	$b\geq50$ $100\leq h\leq350$ $c\geq15$
⑤		$x_1=c/b$ $x_2=b/L$ $x_3=R$ $x_4=\vartheta_1$	$0.2\leq c/b\leq0.6$ $b/t\leq60$ $c/t\leq50$ $h/t\leq500$ $\pi/4\leq\vartheta_1\leq3/4\pi$	$b\geq50$ $100\leq h\leq350$ $c\geq15$ $0.1\leq R\leq0.9$

Table 1
(*continued*)

Prototype	Prototype section	Design variables	Constraints based on EC3	Manufacturing & practical limitations
⑥		$x_1=c/b$ $x_2=b/L$ $x_3=R$ $x_4=\vartheta_1$	$0.2 \leq c/b \leq 0.6$ $b/t \leq 60$ $c/t \leq 50$ $h/t \leq 500$ $\pi/4 \leq \vartheta_1 \leq 3/4\pi$	$b \geq 50$ $100 \leq h \leq 350$ $c \geq 15$ $0.1 \leq R \leq 0.4$
⑦		$x_1=c/b$ $x_2=d/b$ $x_3=b/L$ $x_4=\vartheta_1$	$0.2 \leq c/b \leq 0.6$ $0.1 \leq d/b \leq 0.3$ $b/t \leq 90$ $c/t \leq 60$ $d/t \leq 50$ $h/t \leq 500$ $\pi/4 \leq \vartheta_1 \leq 3/4\pi$	$b \geq 50$ $100 \leq h \leq 350$ $c \geq 15$ $d \geq 5$
⑧		$x_1=c/b$ $x_2=d/b$ $x_3=b/L$ $x_4=R$ $x_5=\theta_1$	$0.2 \leq c/b \leq 0.6$ $0.1 \leq d/b \leq 0.3$ $b/t \leq 90$ $c/t \leq 60$ $d/t \leq 50$ $h/t \leq 500$ $\pi/4 \leq \vartheta_1 \leq 3/4\pi$	$b \geq 50$ $100 \leq h \leq 350$ $c \geq 15$ $d \geq 5$ $0.1 \leq R \leq 0.9$
⑨		$x_1=c/b$ $x_2=d/b$ $x_3=b/L$ $x_4=R$ $x_5=\vartheta_1$	$0.2 \leq c/b \leq 0.6$ $0.1 \leq d/b \leq 0.3$ $b/t \leq 90$ $c/t \leq 60$ $d/t \leq 50$ $h/t \leq 500$ $\pi/4 \leq \vartheta_1 \leq 3/4\pi$	$b \geq 50$ $100 \leq h \leq 350$ $c \geq 15$ $d \geq 5$ $0.1 \leq R \leq 0.4$
⑩		$x_1=\vartheta_1$ $x_2=\vartheta_2$ $x_3=b$ $x_4=c$ $x_5=d$	$h/t \leq 500$ $7/12\pi \leq \vartheta_1 \leq 5/6\pi$ $\pi/4 \leq \vartheta_2 \leq 3/4\pi$ $30 \leq b \leq 48;$ $50 \leq c \leq 60;$ $15 \leq d \leq 60$	$h \geq 100$ $h+2b \cdot \sin\vartheta_1 \leq 350$
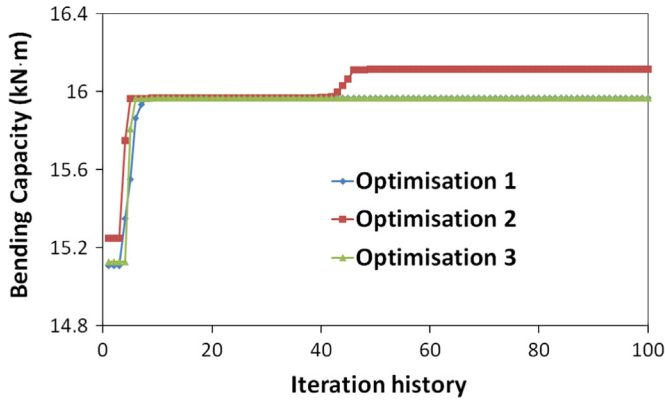
Fig. 8. Iteration history of the maximum bending capacity of prototype ⑩.

lowest bending capacity (one which is even lower than the standard non-optimised section taken as a starting point). This is due to the fact that the flanges without edge stiffeners are highly susceptible to local buckling and, therefore, the strength can only be marginally enhanced by adding intermediate stiffeners to the web in prototype ③. However, the optimised lipped channel section ④ shows that adding an edge stiffener can improve the bending capacity by more than 25%.

Adding an intermediate stiffener in prototype ⑤ increased the bending capacity of the optimum section by only 2%, compared to prototype ④. However, using two intermediate stiffeners in the web (prototype ⑥) actually reduced the flexural capacity of the optimum CFS section by 5.2% compared to the optimum lipped channel with no stiffener (prototype ④). This is due to the fact that folding the intermediate stiffeners into the section (while keeping the total developed length constant) causes a reduction in total height, which impacts negatively on the effective modulus of the section. Moreover, in this symmetric arrangement the web stiffener in the tension zone is completely ineffective. It can be concluded in general terms that for CFS beam sections, edge stiffeners are much more efficient in increasing the section capacity than intermediate web stiffeners.

The results also indicate that, using the same amount of material, the newly developed folded-flange section (prototype ⑩) provides the maximum flexural strength compared to the other prototypes. Moreover, this cross-section can easily be manufactured and satisfies all the practical constraints which were imposed.

It is also noted that the practical constraints imposed on the floor depth h of the sections (listed in the rightmost column of Table 1) never turned out to be critical. However, other practical restraints, in particular the minimum flange width and the restrictions on the ratio R and the angle θ_1, were often found to govern the cross-sectional shape.

5. FE analysis

Detailed geometric and material non-linear FE analyses were performed using ABAQUS [29] to evaluate the flexural behaviour and capacity of the optimised cross-sections for the ten considered prototypes (see Table 2) as well as the standard lipped channel taken as a starting point (Fig. 7). The main purposes of the FE analyses were: (a) to examine the accuracy of the method proposed in Section 2 for the flexural design of folded-flange cross-sections; and (b) to investigate the overall effectiveness of the developed optimisation framework in obtaining sections with increased capacity.

5.1. FE modelling and parameters

The FE models were developed in ABAQUS [29] using the general-purpose S4R element (Fig. 9). This element is a 4-node quadrilateral shell element with reduced integration. Through a sensitivity analysis, a mesh size of 5 mm × 5 mm for the flat plate sections, with smaller elements used in the rounded corner sections was found to be appropriate. No significant change in the ultimate capacity was observed by further reducing the mesh size.

The stress–strain behaviour of the CFS plate material was simulated using the constitutive model proposed by Haidarali and Nethercot [30]. This model is comprised of the basic Ramberg-Osgood stress–strain relationship up to the 0.2% proof stress, followed by a straight line with a constant slope of $E/50$ (where E stands for the initial elastic modulus). Mathematically, the relationship between stress, σ, and strain, ε, is expressed as:

$$\varepsilon = \frac{\sigma}{E} + 0.002\left(\frac{\sigma}{\sigma_{0.2}}\right)^n \qquad for \ \sigma \leq \sigma_{0.2}$$

$$\varepsilon = \varepsilon_{0.2} + \frac{50(\sigma - \sigma_{0.2})}{E} \qquad for \ \sigma \geq \sigma_{0.2} \qquad (14)$$

where $\sigma_{0.2}$ is the 0.2% proof stress, $\varepsilon_{0.2}$ is the total strain at a stress $\sigma_{0.2}$, n is a shape parameter (recommended to be taken as 28 for steel with a yield strength of 350 MPa or 450 MPa [31]) and E was assumed to be equal to 210 GPa.

The effects of geometric imperfections were included in the FE analysis by scaling the local and distortional modes to specific amplitudes and superposing them onto the initial perfect geometry. The cross-sectional deformations of the critical buckling modes were obtained using CUFSM, a finite strip based software [32] and then extruded in the longitudinal direction using a sinusoidal shape with a wavelength equal to the critical wavelength of the relevant mode (although this wavelength was slightly modified to obtain an integer number of half-waves along the member). The magnitudes of the local/distortional geometric imperfections were obtained from the cumulative distribution function (CDF) values presented by Schafer and Pekӧz [33]. In

Table 2
Geometrical details and bending capacities of the optimised sections.

Section	h (mm)	b (mm)	c (mm)	d (mm)	θ_1 (deg)	θ_2 (deg)	R	Bending capacity (kN m)
①	315	50	–	–	–	–	–	9.84
②	305	50	–	–	–	–	0.856	11.08
③	295	50				–	0.186	9.92
Standard (Fig.7)	231	75	17	–	90	–	–	10.30
④	270	50	23	–	91	–	–	13.38
⑤	263	50	21	–	92	–	0.79	13.66
⑥	234	50	20	–	90	–	0.223	12.69
⑦	242	50	29	7.5	90	–	–	15.11
⑧	240	50	25	7	135	–	0.9	14.62
⑨	232	50	25	6.5	135	–	0.1	13.41
⑩	185	48	50	17	105	95	–	16.12

Table 3
Effective cross-sections of the optimised beams, presented at the same scale.

Prototypes	①	②	③	④	⑤
Effective sections					

Prototypes	⑥	⑦	⑧	⑨	⑩
Effective sections					

particular, local and distortional imperfections with a CDF value of 50% were considered, corresponding to values of d_1/t and d_2/t equal to 34% and 94%, respectively, with d_1 and d_2 illustrated in Fig. 10.

To simulate pin-ended boundary conditions with prevented warping (consistent with the assumptions made in the optimisation process), the nodes of each end section of the CFS member were coupled to the central point of the web (acting as the master node) [34]. The external load was then applied in the form of uniform rotations of the end sections about the major axis, using a displacement control regime. The boundary conditions and the applied loading are illustrated in Fig. 9. Large deformation effects were included in the element formulation and a geometric non-linear analysis was carried out in order to be able to accurately track the post-buckling behaviour of the CFS beams. It is worth mentioning that the modelling techniques utilised in this study, including the type of elements, the material behaviour, the meshing and the imperfection modelling borrow heavily from the work by Haidarali and Nethercot [30] and Shifferaw and Schafer [34]. These techniques have been extensively verified against experimental results [35, 36], demonstrating excellent predictive capability with an average error typically less than 4%.

5.2. FE analysis of folded-flange sections with varying dimensions

This section presents the results of FE analyses aimed at evaluating the accuracy of the design approach proposed in Section 2 to calculate the flexural strength of folded-flange CFS cross-sections. To achieve this, six folded-flange sections with a range of different dimensions were investigated. Table 4 provides the geometric details of all selected sections. The ratio b/c of the flange segment lengths (Table 1) and the angles of the inclined lips were
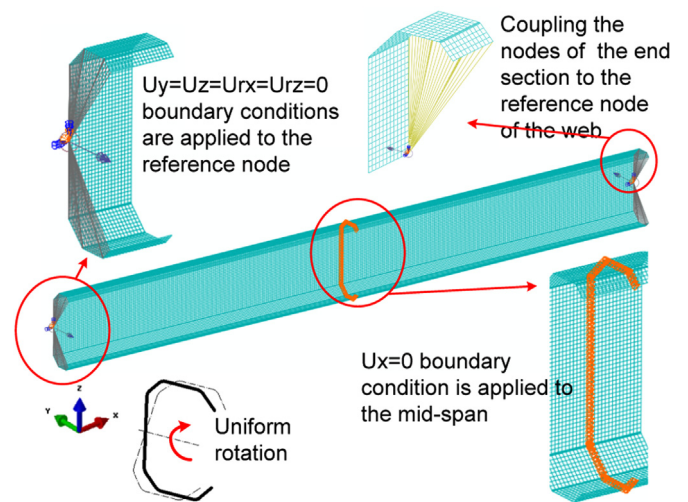
Fig. 9. FE model of the folded-flange beam subjected to local/distortional buckling.

varied. The sections failed by local buckling and/or distortional buckling of the two possible types described in Section 2.2. Since the CFS beams in the current study were laterally restrained, however, lateral-torsional buckling did not occur. As proposed by Galambos [37], the lengths of the FE models were taken as three times the (longest) distortional buckling half-wave length.

The flexural strengths of the selected sections obtained from the FE analyses are compared to those calculated using the proposed design method (Section 2) in Table 4. The results indicate that the proposed design methodology predicts the flexural

Fig. 10. Geometric imperfections: (a) local buckling, and (b) distortional buckling.

capacity of the folded-flange sections with a high degree of accuracy and reliability. The average and the standard deviation of the ratios of the FE results to the EC3 predictions are 1.02% and 8%, respectively, as shown in Table 4.

For illustrative purposes, the effective cross-sections calculated according to EC3, as well as the failed shapes at the ultimate load obtained from the FE analyses, are presented in Table 5. With respect to the effective cross-sections it should be noted that the reduction in thickness of the black lines, in accordance with EC3 philosophy, indicates distortional buckling of the section. These results show that the type 2 distortional buckling mode (see Fig. 6) is dominant for the folded-flange cross-section M2002, where the length of flange segment 1 is around two times the length of segment 2. For all other folded-flange sections in Table 4, distortional buckling of type 1 (see Fig. 5) is critical. This result was predicted by the proposed design methodology and confirmed by the FE analysis results.

The moment-rotation responses of the folded-flange sections obtained from FE analysis are plotted in Fig. 11. It is seen that, with the exception of section M2503, all sections display, to a varying degree, some sort of "snap-back" behaviour past the peak load. This is a phenomenon which is not commonly observed in regular lipped channel sections and is more reminiscent of the post-peak behaviour of, for instance, cylindrical shells or strongly curved plates under compression (Fig. 12). It appears that replacing the semi-circular flange shape in Fig. 2 by a segmental approximation for practical reasons causes the folded-flange section to 'inherit' some of the typical snap-back behaviour of the former.

5.3. FE analysis of optimised cross-sections

The bending moment capacities of the standard channel (Fig. 7) and the optimised prototypes (Table 2) were determined using FE analysis. The adopted boundary conditions were identical to those in the FE models of the folded-flange sections previously

described, and the load was again applied as uniform rotations at both ends. The lengths of the modelled beams (Table 6) were taken as three times the distortional buckling half-wave length. For prototypes without edge stiffeners (prototypes ①, ②, ③) only the local buckling imperfection was incorporated, since local buckling was the dominant mode. Table 6 shows the bending capacities of the optimised and the standard cross-sections obtained from the FE analyses and compares them to those determined based on the EC3 effective width method. Even though the results obtained from EC3 are slightly unconservative compared to the FE predicted capacities, this study shows that the effective width method is generally reliable and provides a reasonable prediction for the bending moment capacities of the selected CFS prototypes. The average ratio of the capacity determined using FEM to the capacity calculated using EC3 was 0.95 with a standard deviation of 5%. The failed shapes at the ultimate load, obtained from FE analysis, are also illustrated in Fig. 13.

6. Comparison of the results and discussion

Fig. 14 compares the EC3 predicted capacities of the optimised sections to the results obtained from detailed FE analysis. As a general conclusion, the FE results follow the trends predicted by EC3 very well and confirm the reliability of the proposed optimisation method. The results also indicate that, for the same amount of material, the optimisation procedure can significantly increase the bending moment capacity of the CFS cross-sections.

It is shown specifically in Fig. 14 that by only optimising the relative dimensions of the plates and the angles of the inclined lips (i.e. prototype ④), the bending capacity of the commercially available channel section taken as a starting point can be increased by more than 30%. A comparison between the optimum results of prototypes ①, ④ and ⑦ indicates that the bending capacity of CFS channel sections can be significantly increased (by up to 55% in this case) by adding edge stiffeners which suppress the distortional mode. On the other hand, comparing the bending capacity of the prototypes ④ and ⑤, and also ⑦ and ⑧, it can be seen that adding intermediate stiffeners in the web does not necessarily increase the optimal bending capacity of the sections. This is also illustrated by the sections with two web stiffeners (prototypes ⑥ and ⑨), where the flexural capacity of the section with stiffeners was up to 13% less than the optimum channel section without web stiffeners (prototype ④). The main reason for this behaviour is that, when placing the stiffener at the centre of the web or in a symmetric arrangement with one stiffener ending up in the tension zone of the beam, the stiffeners are not at their full effectiveness. At the same time, the total developed length of the cross-section is kept constant, so that folding the stiffeners into the section reduces the total height of the cross-section and, therefore, its bending capacity. For practical reasons, however, it is not

Table 4
Dimensions of the folded-flange cross-sections and bending capacity obtained from EC3 and FEM.

Sections	Thickness (mm)	Depth (mm)	θ_1 (deg)	θ_2 (deg)	Flange1 b (mm)	Flange2 c (mm)	Lip d (mm)	Corner radius (mm)	Capacity (kN·m)		FEM/EC3
									EC3	FEM	
M2001	1.4	200	135	135	18	66	18	2.8	10.14	10.06	0.99
M2002	1.4	200	135	135	66	30	18	2.8	13.74	15.20	1.11
M2003	1.4	200	135	135	40	40	18	2.8	12.71	11.77	0.93
M2501	1.6	250	135	135	18	85	18	3.2	16.50	15.09	0.91
M2502	1.6	250	120	90	30	61	30	3.2	19.76	21.30	1.08
M2503	1.6	250	150	45	30	61	30	3.2	19.43	21.11	1.09
Average Standard deviation											1.02 0.08

Table 5
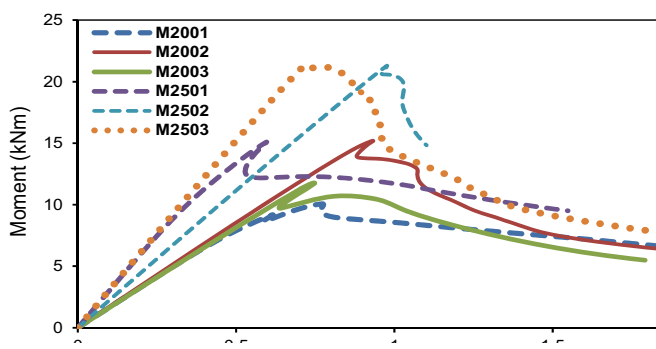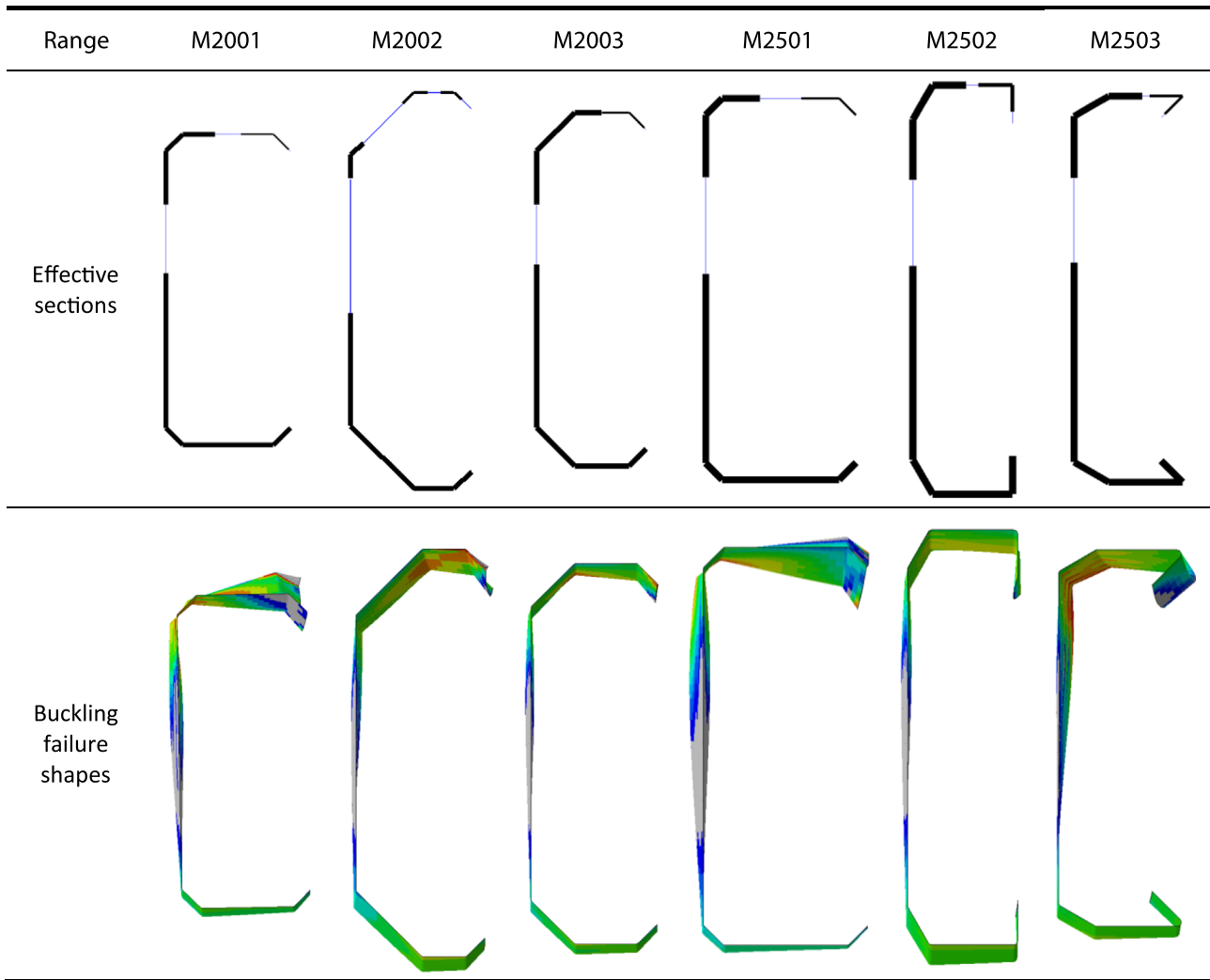Effective cross-sections and buckled shapes of the folded-flange beams (presented at a consistent scale).

Range	M2001	M2002	M2003	M2501	M2502	M2503
Effective sections						
Buckling failure shapes						

Fig. 11. Moment-rotation curve of the folded-flange sections.

Fig. 12. Schematic view of the behaviour of axially compressed panels (adapted from [38]).

recommended to place the stiffeners in an asymmetric configuration since errors during the installation of the beams would almost be inevitable. Fig. 14 also highlights the increased efficiency of the proposed folded-flange prototype compared to any other prototype considered. It is shown that, for the same amount of material, prototype ⑩ leads to a maximum flexural capacity which is around 57% higher than the standard commercially available

channel section and 22% higher than the optimum lipped channel section (prototype ④). Folded-flange sections are also easy to manufacture and connect to typical floor systems and, hence, are ideal candidates for practical CFS beam sections.

Table 6
Comparison of the bending moment capacities of the optimised and standard sections obtained from EC3 and FE analysis.

Section	Buckling half-wave lengths		Modelling length (mm)	Bending moment capacity (kN m)		FEM/EC3
	Local (mm)	Distortional (mm)		EC3	FEM	
Standard channel	100	600	1800	10.3	10.4	0.99
①	200	–	600	9.84	9.11	1.08
②	200		600	11.08	11.22	0.99
③	200	–	600	9.92	9.41	1.05
④	140	600	1800	13.38	12.73	1.05
⑤	50	600	1800	13.66	12.08	1.13
⑥	50	600	1800	12.69	11.15	1.14
⑦	120	800	2400	15.11	14.09	1.07
⑧	100	800	2400	14.62	12.99	1.13
⑨	100	800	2400	13.41	12.33	1.09
⑩	100	800	2400	16.12	15.52	1.04
Average						0.95
Standard deviation						0.05

## 7. Summary and conclusions

In this paper, a practical framework is proposed to optimise CFS beam cross-sections while considering code-based design constraints as well as manufacturing issues and practical limitations. Using the framework, a commercially available CFS lipped channel section was optimised based on ten different prototypes, including a folded-flange cross-section, while keeping the material use constant. A slight modification of the EC3 design methodology was first developed in order to account for the multiple distortional buckling modes which may occur in the folded-flange cross-section. The particle swarm optimisation algorithm was then used to
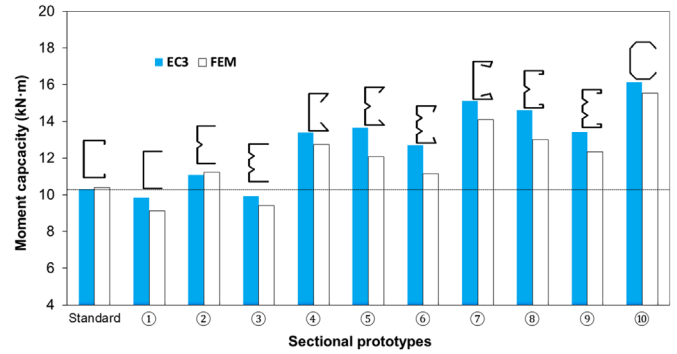
Fig. 14. Comparison of the moment capacities of different prototypes.

obtain the solutions with the maximum flexural strength. The accuracy of the modified design model and the effectiveness of the proposed optimisation framework were also evaluated using detailed non-linear FE analysis. The following conclusions can be drawn:

- The FE simulations of the folded-flange sections confirm that the proposed additions to the effective width based design method in EC3 to account for the multiple distortional buckling modes in the folded-flange section lead to accurate predictions of the ultimate bending capacity.
- By applying the proposed optimisation framework to laterally braced beams, the bending capacity of a commercially available CFS beam was increased by 30% by only optimising the relative dimensions of the flat plates and the inclination of the lips. The results also indicate that flanges with double fold lips have the potential to considerably increase the flexural capacity of CFS beams (by up to 50%), while using intermediate stiffeners in the web does not necessarily increase the capacity of the sections. As expected, plain CFS channel cross-sections provided the
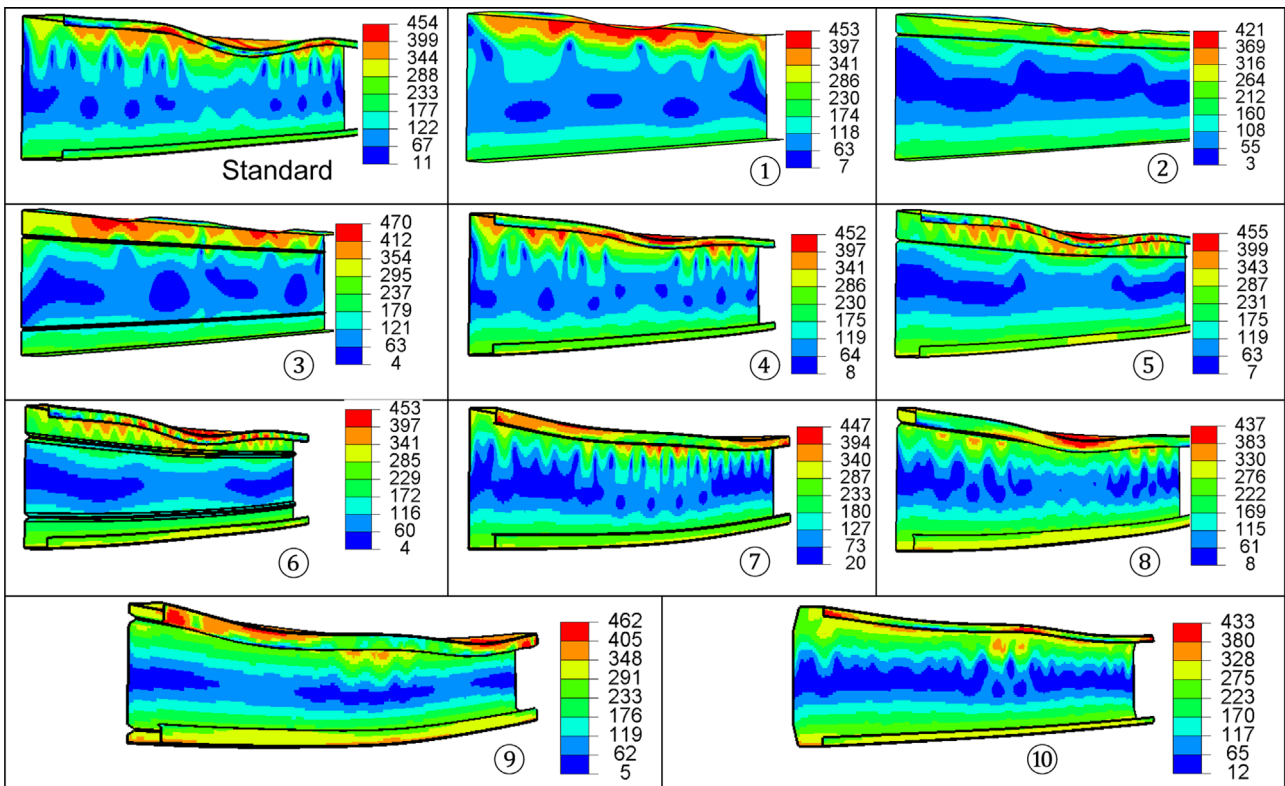
Fig. 13. Failed shapes of optimised and standard sections.

minimum flexural capacity, even when adding intermediate web stiffeners.

- Folded-flange sections, which can be easily designed and manufactured due to their simple sequence of straight plate segments with a relatively small number of folds, are shown to be viable and even superior alternatives to typical lipped channel sections. For the same amount of material (i.e. the same total coil width and plate thickness), the folded-flange section possesses a flexural capacity which is 57% and 22% higher than the selected commercial section and the optimum lipped channel section, respectively.

Acknowledgement

References

[1] L. Fiorino, O. Iuorio, R. Landolfo, Designing CFS structures: the new school bfs in naples, Thin Wall Struct. 78 (2014) 37–47.
[2] J.B.P. Lim, D.A. Nethercot, Finite element idealization of a cold-formed steel portal frame, J. Struct. Eng. – ASCE 130 (2004) 78–94.
[3] J.B.P. Lim, D.A. Nethercot, Ultimate strength of bolted moment-connections between cold-formed steel members, Thin Wall Struct. 41 (2003) 1019–1039.
[4] J. Lee, S.M. Kim, H.S. Park, Y.H. Woo, Optimum design of cold-formed steel channel beams using micro genetic algorithm, Eng. Struct. 27 (2005) 17–24.
[5] Y.S. Tian, T.J. Lu, Minimum weight of cold-formed steel sections under compression, Thin Wall Struct. 42 (2004) 515–532.
[6] J.H. Lee, S.M. Kim, H.S. Park, Optimum design of cold-formed steel columns by using micro genetic algorithms, Thin Wall Struct. 44 (2006) 952–960.
[7] H. Adeli, A. Karim, Neural network model for optimization of cold-formed steel beams, J. Struct. Eng.-ASCE 123 (1997) 1535–1543.
[8] K. Magnucki, M. Maćkiewicz, J. Lewiński, Optimal design of a mono-symmetrical open cross section of a cold-formed beam with cosinusoidally corrugated flanges, Thin Wall Struct. 44 (2006) 554–562.
[9] K. Magnucki, M. Rodak, J. Lewiński, Optimization of mono- and anti-symmetrical I-sections of cold-formed thin-walled beams, Thin Wall Struct. 44 (2006) 832–836.
[10] E. Magnucka-Blandzi, Effective shaping of cold-formed thin-walled channel beams with double-box flanges in pure bending, Thin Wall Struct. 49 (2011) 121–128.
[11] W. Ma, J. Becque, I. Hajirasouliha, J. Ye, Cross-sectional optimization of cold-formed steel channels to Eurocode 3, Eng. Struct. 101 (2015) 641–651.
[12] J. Ye, I. Hajirasouliha, J. Becque, A. Eslami, Optimum Design of Cold-formed Steel Beams Using Particle Swarm Optimisation Method, J. Constr. Steel Res., 2015, (in preparation).
[13] CEN, Eurocode 3: Design of Steel Structures, Part 1.3: General Rules—Supplementary Rules for Cold-formed Steel Members and Sheeting, in, Brussels: European Comittee for Standardization, 2005.
[14] AISI, North American Specification for the Design of Cold-formed Steel Structural Members, 2007 Edition, in: AISI S100-07, Washington, DC, 2007.
[15] J.Z. Leng, J.K. Guest, B.W. Schafer, Shape optimization of cold-formed steel columns, Thin Wall Struct. 49 (2011) 1492–1503.
[16] B.P. Gilbert, T.J.M. Savoyat, L.H. Teh, Self-shape optimisation application: optimisation of cold-formed steel columns, Thin Wall Struct. 60 (2012) 173–184.
[17] H. Liu, T. Igusa, B.W. Schafer, Knowledge-based global optimization of cold-formed steel columns, Thin Wall Struct. 42 (2004) 785–801.
[18] J.Z. Leng, Z.J. Li, J.K. Guest, B.W. Schafer, Shape optimization of cold-formed steel columns with fabrication and geometric end-use constraints, Thin Wall Struct. 85 (2014) 271–290.
[19] A.B. Sabbagh, M. Petkovski, K. Pilakoutas, R. Mirghaderi, Development of cold-formed steel elements for earthquake resistant moment frame buildings, Thin Wall Struct. 53 (2012) 99–108.
[20] CEN, Eurocode 3: Design of Steel Structures. Part 1-1: General Rules and Rules for Buildings, in, Brussels: European Comittee for Standardization, 2005.
[21] CEN, Eurocode 3: Design of Steel Structures, part 1-5: Plated Structural Elements, in, Brussels: European Comittee for Standardization, 2005.
[22] AS/NZS, Cold-formed Steel Structures, in, Sydney: AS/NZS 4600, Joint Technical Committee BD-082, 1996.
[23] Swarm Intelligence for Multi-objective Problems in Data Mining, Stud Comput Intell, 242, 2009, 1-287.
[24] R. Hassan, B. Cohanim, O. De Weck, G. Venter, A comparison of particle swarm optimization and the genetic algorithm, in: Proceedings of the 1st AIAA Multidisciplinary Design Optimization Specialist Conference, 2005, pp. 18–21.
[25] S. Jeong, S. Hasegawa, K. Shimoyama, S. Obayashi, Development and investigation of efficient GA/PSO-hybrid algorithm applicable to real-world design optimization, IEEE Comput. Intell. Mag. 4 (2009) 36–44.
[26] R.E. Perez, K. Behdinan, Particle swarm approach for structural design optimization, Comput. Struct. 85 (2007) 1579–1588.
[27] Y. Shi, R. Eberhart, A modified particle swarm optimizer, in: Evolutionary Computation Proceedings, 1998. IEEE World Congress on Computational Intelligence., The 1998 IEEE International Conference on, IEEE, 1998, pp. 69–73.
[28] Mathworks, Matlab R2011a, in, Mathworks, Inc, 2011.
[29] ABAQUS, in, Hibbitt, Karlsson & Sorensen, Inc, Pawtucket, USA, 2007.
[30] M.R. Haidarali, D.A. Nethercot, Finite element modelling of cold-formed steel beams under local buckling or combined local/distortional buckling, Thin Wall Struct. 49 (2011) 1554–1562.
[31] L. Gardner, M. Ashraf, Structural design for non-linear metallic materials, Eng. Struct. 28 (2006) 926–934.
[32] B. Schafer, CUFSM Version 3.12, in, Department of Civil Engineering, Johns Hopkins University, 2006. ⟨http://www.ce.jhu.edu/bschafer/cufsm/⟩.
[33] B.W. Schafer, T. Pekoz, Computational modeling of cold-formed steel: characterizing geometric imperfections and residual stresses, J. Constr. Steel Res. 47 (1998) 193–210.
[34] Y. Shifferaw, B.W. Schafer, Inelastic Bending Capacity of Cold-Formed Steel Members, J. Struct. Eng.-ASCE 138 (2012) 468–480.
[35] C. Yu, B.W. Schafer, Local buckling tests on cold-formed steel beams, J. Struct. Eng. – ASCE 129 (2003) 1596–1606.
[36] C. Yu, B.W. Schafer, Distortional buckling tests on cold-formed steel beams, J. Struct. Eng. – ASCE 132 (2006) 515–528.
[37] T.V. Galambos, Guide to Stability Design Criteria for Metal Structures, John Wiley & Sons, USA, 1998.
[38] R.M. Jones, Buckling of Bars, Plates, and Shells, Bull Ridge Corporation, USA, 2006.